Bulletin of Volcanology (2025) 87:111
https://doi.org/10.1007/s00445-025-01901-5

RESEARCH ARTICLE

Analysis of the 2022 HTHH eruption cycle using geostationary satellite thermal infrared spectroscopy

James O. Thompson[1] · Daniel B. Williams[2] · Vincent J. Realmuto[3] · Michael S. Ramsey[2,3]

Received: 1 August 2025 / Accepted: 12 October 2025

Abstract

On 15 January 2022, the Hunga Tonga–Hunga Ha'apai (HTHH) volcano generated a large sulfur dioxide (SO_2), water vapor (H_2O), and silicate (SiO_4) ash plume that rapidly rose to a maximum height of ~58 km. The GOES-17 Advanced Baseline Imager (ABI) acquired continuous, high-temporal-cadence, thermal infrared (TIR) data providing the ability to both examine precursory thermal activity and track the eruption plume's migration. The above background temperatures began to increase on 20 December 2021, with a maximum of 7.2 K detected on 8 January, leading up to the larger eruption on 14–15 January 2022. TIR spectral deconvolution modeling of the initial plume was performed to map the ash composition, particle size distribution (PSD), and ice formation. Several glass-rich andesite spectral endmembers provided the best match, with significant water vapor also detected, likely a result of vapor expansion driving the eruption and the source of ice formation at higher altitudes. The initial chaotic PSD became organized over time as the larger particles fell out of suspension leaving the fines plus water ice dominating as the plume drifted west. Over the next 1–3 days of the eruption, the diffuse plumes were dominated by SO_2 and fine ash, which allowed a different modeling approach to retrieve SO_2 column density and sulfate speciation. The high-temporal-resolution ABI data provided an opportunity to couple pre-, syn-, and post-eruption thermal dynamics to understand large, water-rich submarine explosive eruptions and plume evolution.

Key points:

- High-temporal-resolution thermal infrared data enabled a complete analysis of the eruption.
- Thermal anomalies are seen prior to the large eruption in January 2022.
- Ash was tracked during the initial ~17 h of the climactic explosive eruption followed by SO_2.

Keywords Thermal Infrared · Emissivity · Geostationary · Hunga Tonga–Hunga Ha'apai · Volcanic Ash Mapping · SO2 Detection

Introduction

The Hunga Tonga–Hunga Ha'apai (HTHH) volcano experienced an explosive phreatoplinian eruption on 14–15 January 2022, which rapidly lofted significant quantities of volcanic ash and gas into the Mesosphere (maximum height of 58 km above mean sea level) (Proud et al. 2022; Yuen et al. 2022) and created the greatest measured stratospheric aerosol optical depth since the 1991 eruption of Pinatubo (Taha et al. 2022). The 14-15 January eruption was preceded by two Surtseyan eruptions, first recorded on 19 December 2021 (Carr et al. 2022). The 2022 activity was also defined by the large quantities of water vapor that were injected into the atmosphere, estimated at ~146 Tg (Millán et al. 2024), which can affect aerosol conversion rates in the plume (Zhu et al. 2022). Estimates for the amount of SO_2 released by the 2022 eruption range from 0.5 to 1.5 Tg (Carn et al. 2022; Sellitto et al. 2024), and the combination of both sulfate aerosols and water vapor was shown to have caused contrasting effects on the Earth's climate over the period between the eruption and the end of 2023. Schoeberl et al. (2024)

Editorial responsibility: M. Edmonds

James O. Thompson
james.thompson@beg.utexas.edu

[1] Bureau of Economic Geology, The University of Texas at Austin, Austin, TX 78712, USA

[2] Department of Geology and Environmental Science, University of Pittsburgh, Pittsburgh, PA 15260, USA

[3] Jet Propulsion Laboratory, California Institute of Technology, Pasadena, CA, USA

Published online: 08 November 2025

suggested that tropospheric warming by stratospheric water vapor was offset by the cooling effect of sulfate aerosols. Aerosol particle sizes measured by Boichu et al. (2023) also suggest a net radiative cooling effect, which has been observed causing changes to both the chemistry and circulation of the stratosphere (Wilmouth et al. 2023).

Hunga Tonga and Hunga Ha'apai are the subaerial island remnants of a large (~6 km diameter) andesitic submarine caldera, located about 58 km north of Tongatapu (Bryan et al. 1972). These islands are composed of gently dipping alternating layers of andesite lavas, ash, scoria, and lapilli. Previous submarine eruptions in the area were reported in 1912, 1937, 1988, 2009, and 2014–2015, with some producing subaerial deposits (Bryan et al. 1972; Cronin et al. 2017; Brenna et al. 2022). For example, the December 2014–January 2015 eruption formed a land bridge between Hunga Tonga and Hunga Ha'apai. The eruptions in late 2021 dramatically reshaped the morphology of the islands prior to the major explosive eruption in January 2022. This sequence of eruptions ejected large quantities of material into the atmosphere, leaving only small subaerial remnants of the islands above sea level (Cronin et al. 2017; Brenna et al. 2022).

Analysis of any plume-forming eruption requires timely collection of data to capture the highly dynamic processes and inform predictive eruption and dispersion models as well as thermal detection algorithms. High-temporal-resolution thermal infrared (TIR) data from geostationary satellites can provide such data but have not been routinely utilized in the past for volcano/eruption monitoring. However, these data are critical for the timely collection and long-term insights into dynamic volcanic processes and eruptive mechanisms (e.g., Thompson et al. 2022). For this study, we leverage TIR observations acquired by the Advanced Baseline Imager (ABI) to both document the increase in surface temperature that preceded the climactic HTHH eruption together with systematic analysis of the eruption plume/cloud composition and ash particle size in the ~17 h following that eruption. The high-temporal-resolution (~10 min) data provide a unique opportunity to develop more comprehensive long-term thermal trends and observe the dynamic processes within the plume. This cadence also minimizes the effect of meteoric clouds on observations, with greater opportunity for clear sky views of the sea and plume surface. Clouds can have a larger impact on the data from polar orbiting infrared datasets, such as the Advanced Spaceborne Thermal Emission and Reflection Radiometer (ASTER), where repeat observations are typically 5–16 days apart. Therefore, one or two scenes with obscuring clouds results in no data for a month, which is especially common in the tropics and later in the day (Ramsey and Flynn 2020).

Currently, 24 active volcanoes are being monitored by a NASA-funded program called the Geostationary Urgent Request Protocol (GEO-URP) over the spatial extent of the GOES and Himawari TIR instruments (http://ivis.eps.pitt.edu/GOES/). By linking data from polar and geostationary observations, the results improve the detection of high-frequency thermal fluctuations and precursory trends. The GEO-URP System for volcanic observations evolved from the ASTER Urgent Request Protocol (URP) system (Ramsey 2016). That system was originally conceived in 2004 and implemented as a synergistic approach to leverage ongoing operational volcanic monitoring programs in order to improve the number of ASTER acquisitions of every active volcano. The system relied on high temporal/low spatial resolution satellites like AVHRR and MODIS to trigger (and eventually automate) the ASTER expedited data system, specifically for volcano monitoring and science (Ramsey 2016; Ramsey and Flynn 2020). After the ASTER Emergency Scheduling Interface and Control System (AESICS) system, operated by the Land Processes Distributed Active Archive Center (LP DAAC), receives an automated volcanic thermal trigger, the GEO-URP automated system is activated and retrieves the prior 18 months of ABI full disk data from the Amazon Web Services (AWS) National Oceanic and Atmospheric Administration (NOAA) data server. These images are spatially trimmed to a smaller region around the triggered volcano. The data are then automatically processed to remove those scenes obscured by meteoric clouds as well as those with any non-volcanic anomalies. A thermal baseline is established and thermal fluctuations at the volcano are identified (Girona et al. 2021; Thompson et al. 2022). Time series analyses are conducted to detect any precursory thermal activity over the 18 months leading up the date of the URP trigger. Additionally, spatial analysis is conducted using thermal and decorrelation stretches (Fig. 1) at given time periods. For the detection of new thermal activity at a volcano, the entire historical analysis from the initial trigger to production of the complete time series of images takes less than 5 days. However, after a volcanic eruption has been initially integrated into the system it is updated daily until the activity has subsided. This enables near real-time monitoring, modeling, and forecasting of lava and ash/SO_2 plumes at high temporal resolution (e.g., Thompson et al. 2022).

In this study, we analyzed the GEO-URP data related to the HTHH eruption but then expanded outward to a larger region of interest in order to analyze the thermal and compositional trends of the drifting volcanic clouds. Thermal analysis of the HTHH islands and surrounding ocean revealed precursory activity and potential submarine activity, as well as the development of new subaerial volcanic deposits. A more detailed analysis of the opaque (proximal) region of the rising and drifting ash plume allowed us to determine the composition and particle size using spectral linear deconvolution modeling, first demonstrated on ASTER data (Williams and Ramsey

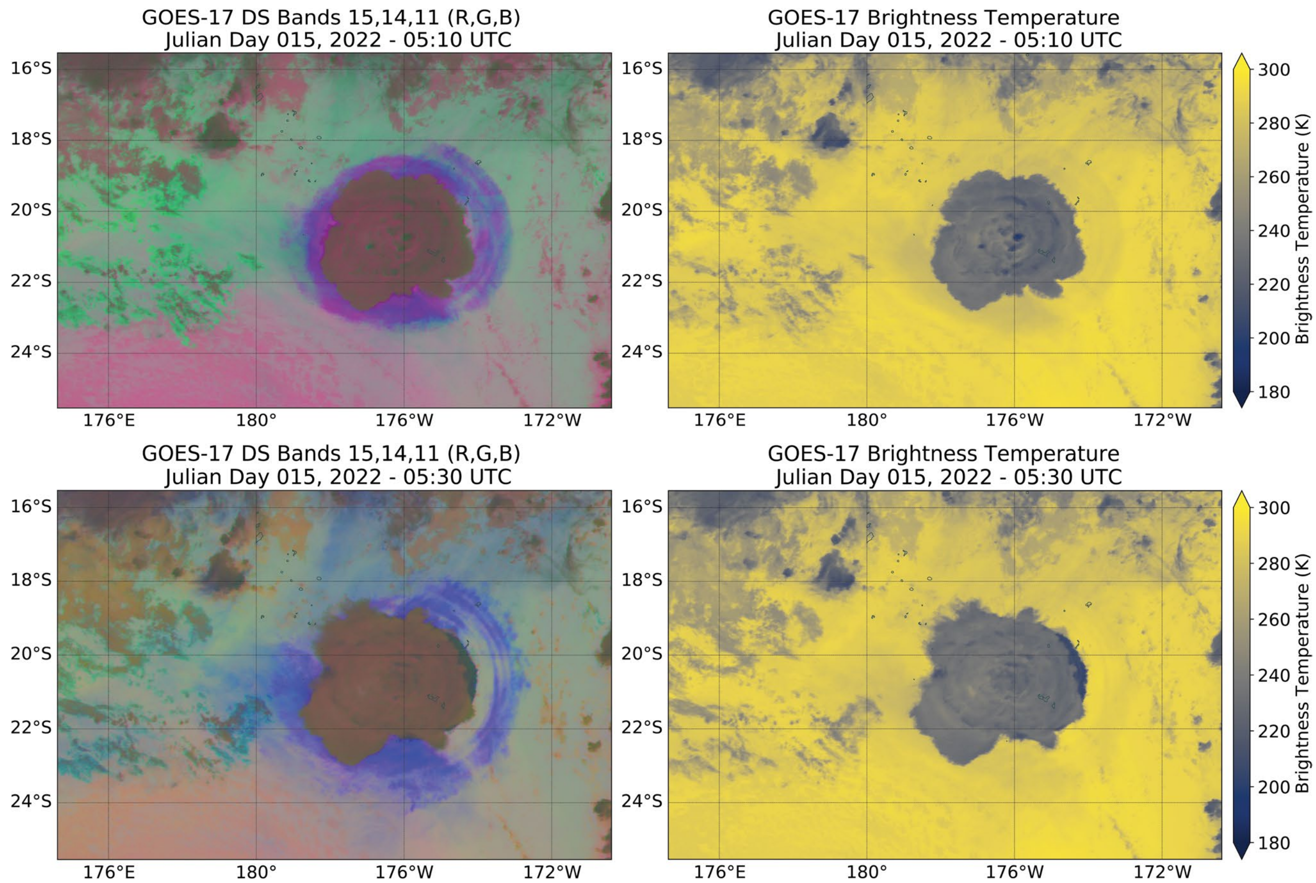

Fig. 1 Derived thermal infrared properties of the rising and expanding volcanic plume from HTHH on 15 January 2022 at 5:10 (top row) and 5:30 (bottom row) UTC. Decorrelation stretches (left column) of GOES ABI radiance bands 15, 14, and 11 (R, G, B) show the rapid transition of water vapor (liquid) to ice on the outer portions of the umbrella cloud during ascent into the atmosphere. Brightness temperatures (right column) calculated using GOES ABI radiance band 14 show the rapid cooling of the rising plume, epically at the top and center. However, the outer portions of the umbrella cloud remain close to freezing temperatures

2019, 2022). These properties cannot be determined in this part of the plume by any other modeling approach such as transmission-based ash retrieval algorithms (e.g., Pavolonis et al. 2013). Notably though, these proximal plume properties can serve as input into such transmission models (e.g., “Plume Tracker”; Realmuto and Berk 2016) used for SO_2 and ash detection in the more distal, diffuse plume.

Methodology

As part of the GOES-URP program, several data products are generated from the Advanced Baseline Imager multispectral TIR radiance data, which include surface temperature and emissivity from all six TIR bands, surface temperature and radiant heat flux time series, ash particle size and composition maps, as well as SO_2 and ash index images. The following sections describe these data products in more detail.

Advanced Baseline Imager processing

The Advanced Baseline Imager on GOES-17 acquires 16 radiance measurements between band centers of 0.47 and 13.3 μm at a spatial resolution of 0.5–2 km and temporal resolution of 10 min (Schmit et al. 2017). This study uses six TIR bands (8.4, 9.6, 10.3, 11.2, 12.3, and 13.3 μm) with a spatial resolution of 2 km at nadir. The spectral and temporal resolution of the instrument allows the observation, analysis, and interpretation of highly dynamic thermal and compositional volcanic processes, including those ongoing in the 2022 HTHH eruption plume. The L1 TIR radiance bands are combined, georeferenced, and subsampled to a smaller geographical extent (approximately 550-km radius) around the HTHH volcano. The L1 radiance data are then separated into surface kinetic temperature and emissivity using the Temperature-Emissivity Separation (TES) algorithm developed for ASTER and modified to use the ABI spectral response functions (Gillespie et al. 1998; Thompson et al. 2022). These data are then used for the science analysis presented here.

Thermal time series

The temperature and radiant heat flux time series pre-, syn-, and post-eruption is produced for the entire sequence of HTHH eruptions from 12 November 2021 until 1 February 2022. This time series is generated by first removing any scenes with significant meteoric cloud and then applying a 2-sigma percentile removal of the remaining data, based on methodologies of previous similar studies to remove any outliers (e.g., Lundgren et al. 2020; Girona et al. 2021; Thompson et al. 2022). An additional 1-sigma percentile lowpass filter is performed over a daily and sub-weekly period to eliminate diurnal fluctuations (Thompson et al. 2022). The temperature time series is then created from any detected anomalous pixels and their associated values above the average background temperature are logged. The radiant heat flux/power (watts) from the surface is calculated (Eq. 1) from the measured spectral emissivity (ε_λ), surface temperature (T_s), and ambient/background surface temperature (T_a):

$$\phi_{tot} = \left\{\left[\varepsilon_\lambda \cdot \sigma\left(T_s^4 - T_a^4\right)\right]\right\} \cdot A \quad (1)$$

where σ is the Stefan–Boltzmann constant and A is pixel area (Harris 2013; Thompson and Ramsey 2020).

The analysis of volcanic ash clouds from geostationary sensors has primarily focused on tracking their height and location in the atmosphere, along with properties such as mass and effective particle radius (Elrod et al. 2003; Pavolonis et al. 2013; 2020). This has been performed using methods that utilize the Mie Scattering properties of volcanic ash in two or more TIR spectral bands (e.g., Prata 1989; Pavolonis et al. 2015a, b). However, these methods rely on a transmissive plume upwelling TIR radiation from the Earth's surface, and an assumed ash composition must be used to understand the scattering properties of cloud. The pitfalls of this kind of analysis have been well described in the literature regarding both cloud detection in TIR data (Simpson et al. 2000; Prata et al. 2001) and the calculation of cloud properties, such as the mass, altitude, and plume opacity (Mackie et al. 2014). Our analysis uses a two-stage approach for modeling the proximal, opaque and the distal, transmissive regions of the plume/cloud.

Opaque plume modeling (SiO_4 ash and H_2O)

The opaque region is generally ignored by standard radiative transfer (RT) algorithms due to the high optical depth (OD) in this region that blocks all emission from the ground below. Williams and Ramsey (2019, 2022) demonstrated the use of coupled TIR emission spectroscopy of volcanic ash and linear spectral deconvolution modeling of ASTER TIR data to retrieve both the composition and particle sizes present within opaque ash clouds. Here, we apply the same methods to the GOES emissivity product, calculated using the Temperature Emissivity Separation (TES) algorithm (Gillespie et al. 1998).

Deconvolution modeling of TIR image data requires a spectral library of endmembers as input, typically compiled from high-resolution laboratory data. Here, we use the ASTER volcanic ash library (AVAL) developed by Williams and Ramsey (2019). This library of ash samples contains different petrologic compositions divided into distinct particle size fractions through a combination of sieving and aerodynamic settling using a Microorifice Uniform Deposit Impactor (MOUDI). Different size fractions are needed to account for diffraction-induced spectral "transparency features" that emerge in particles < 63 µm in diameter (Conel 1969; Ramsey and Christensen 1998). Emissivity spectra are collected using a Nexus Nicolet 670 FTIR spectrometer with the two-temperature approach to calibration (Ruff et al. 1997). Spectra in each volcanic suite are resampled to the TIR wavelengths of the sensor of interest (e.g., ASTER or here, GOES ABI) (Fig. 2). We also acquired the spectrum of water ice from the ECOSTRESS spectral library to use in our image analysis (Meerdink et al. 2019). Given the large quantities of water vapor that was released during the HTHH eruption (Vömel et al. 2022) and the height that this plume reached in the atmosphere, it was assumed that ice crystallization could mask the spectrum of ash, leading to inaccurate results from spectral modeling.

The ABI L1 radiance data are processed through the TES algorithm (Gillespie et al. 1998), producing analogous data products to those of ASTER—surface temperature and a six-band emissivity file. The resampled ash spectra (Fig. 2) are used as the end-member library for the spectral deconvolution modeling (Ramsey and Christensen 1998). Each TIR ABI mixed-pixel spectrum is modeled using a linear combination proportional to the areal percentage of each endmember. The linear model then calculates the best possible fit of each endmember spectrum to the pixel spectra found in TIR ABI data resulting in a fractional percent of each endmember for each pixel. Per-pixel root mean square (RMS) error is also calculated to determine the "goodness of fit" of the modeled spectrum.

The model used here is only applicable where the plume is opaque to upwelling ground radiance behaving essentially as an emitting ground surface. To determine the extent of the opaque portion and where the model would no longer be considered applicable, the optical depth (OD) of each pixel is calculated using the methods of Garnier et al. (2013):

$$\mathrm{OD} = -\ln\left[1 - \frac{\mathrm{R_s} - \mathrm{R_m}}{\mathrm{R_s} - \mathrm{B_a}}\right] \quad (2)$$

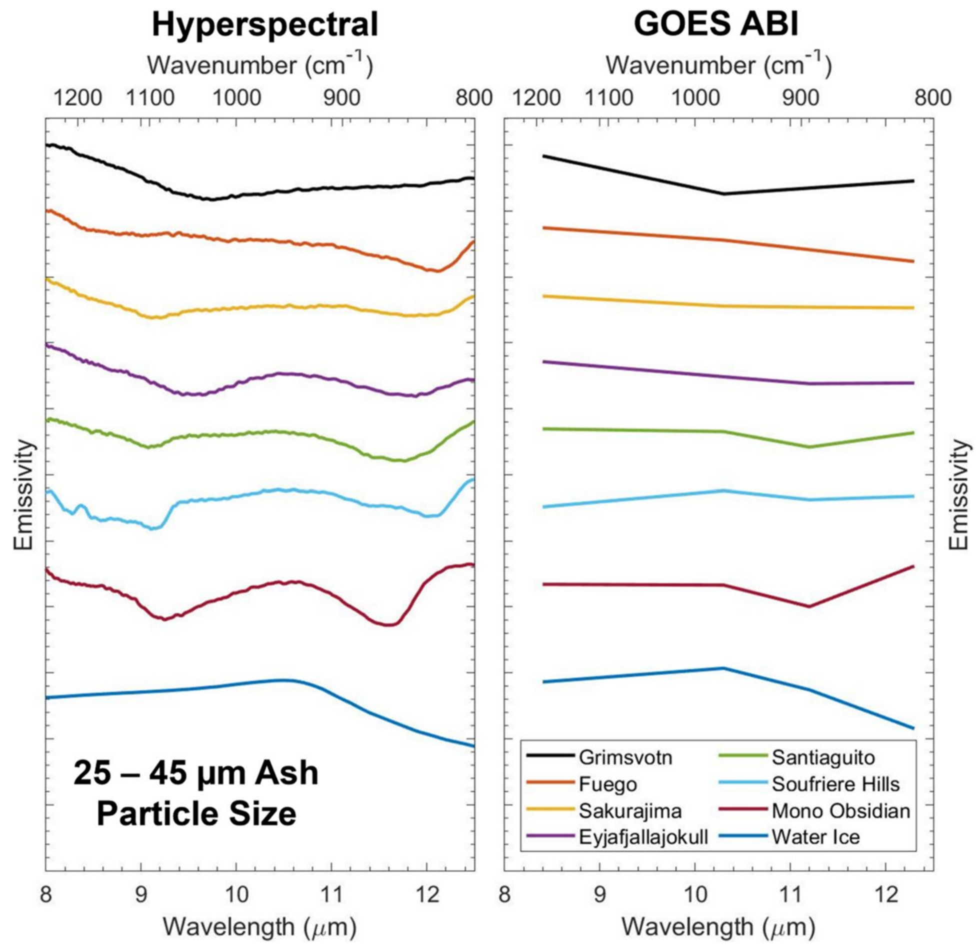

Fig. 2 Example spectra from the ASTER Volcanic Ash Library (Williams and Ramsey 2019) at (left) hyperspectral and (right) GOES ABI resolution (spectral offset vertically for clarity). Despite there being greater similarities in the GOES spectra compared to those acquired in the laboratory, the spectral differences are significant enough in both the ash and water ice samples, particularly at longer wavelengths, to accurately deconvolve GOES image data

where R_s is ~ 11 µm surface radiance, R_m is 11 µm per-pixel radiance, and B_a is plume top Planck radiance. In this calculation, we assume that the plume is opaque where the temperature of the plume pixel is at or near equilibrium with the temperature of the surrounding atmosphere. The multi-layered structure of the HTHH plume does pose some difficulties in this calculation, owing to the umbrella cloud shape as well as central dome, over which there was a height difference of ~ 30 km (Proud et al. 2022). This is also beyond the measurement limit of radiosonde data that have been used previously in this kind of analysis (e.g., Williams and Ramsey 2022).

Therefore, a slightly different approach was taken compared to previous studies of smaller ash plumes. Stereoscopic measurements have been previously used to calculate the plume height using a combination of both GOES and Himawari data (Carr et al. 2022; Proud et al. 2022). We compared these heights to the temperature at each cloud height using the Modern-Era Retrospective Analysis for Research and Applications (MERRA-2) reanalysis of the 3-h vertical temperature product. This is generated from the Goddard Earth Observing System Model, produced with the Giovanni online data system, which is developed and maintained by the NASA Goddard Earth Sciences Data and Information Services Center (GES DISC; Acker and Leptoukh 2007). From this, OD was calculated for the different height regions of the plume to determine opacity at each height. We used the estimate of OD ≥ 4 as the threshold for opaque plume pixels (Rose et al. 1995). Values below this OD threshold are masked and not modeled using the linear deconvolution approach. We further confirmed the opacity by calculating the brightness temperature difference of the plume between ABI channels 12 and 13. Where a plume is optically opaque to ground upwelling radiance, the brightness temperature difference should theoretically be ~ 0 K (Prata and Grant 2001).

Diffuse plume modeling (SO_2 and aerosols)

The opaque plume modeling does not account for SO_2 or other volcanic gases and aerosols, which are generally best detected in diffuse plumes that transmit the radiance from the ground or water surface below the plume. This modeling is also sensitive to the presence of ash, but not the composition or particle size. The detection of SO_2 and ash in diffuse volcanic clouds is based on three data products: the maximum brightness temperature (BT_{max}), the SO_2 index, and the ash index, generated from the ABI multispectral TIR radiance measurements in channels 11 (centered at 8.44 µm), 13 (10.33 µm), 14 (11.19 µm), and 15 (12.27 µm). The BT_{max} is the maximum brightness temperature of the four ABI channels and, for a given line of sight (LOS), represents the channel least affected by atmospheric transmission and surface emissivity. The SO_2 index (Krotkov et al. 2021) is the scaled difference between the brightness temperature at 8.44 µm and the BT_{max} and represents the strength of SO_2 absorption. The ash index is the scaled difference between the BT at 11.19 µm and the BT_{max} and represents the strength of ash absorption. We note that absorption is a function of the concentration of SO_2 or ash and the temperature contrast between a plume and the underlying radiating surface, and more computationally intensive radiative transfer (RT) modeling is required to estimate the actual concentrations.

The SO_2 index serves to target the RT modeling at the LOS, which is most likely to pass through the SO_2 plumes. Our quantitative estimates of SO_2 column density are based on the spectral transmission of SO_2 in the 8–13 µm atmospheric window. With respect to the ABI channels, SO_2 absorption is restricted to channel 11 (8.44 µm) and the SO_2 clouds are transparent in channels 13, 14, and 15. We exploit this transparency to estimate the temperature of the radiating surface beneath the plumes and then use this temperature to estimate the SO_2 concentration required to produce the absorption observed in channel 11 (Ackerman et al. 2008; Realmuto and Berk 2016, and references therein).

Results

High-temporal-resolution GOES ABI TIR data enabled detailed thermal and compositional analyses retrospective to and throughout the 2022 Hunga Tonga–Hunga Ha'apai eruption. Temperatures at the target began to exceed the thermal background in late November 2021, weeks before the larger eruptions. A significant increase in thermal anomalies was then observed on 20 December 2021, corresponding to the Surtseyan eruptions at the time (Fig. 3), and the maximum

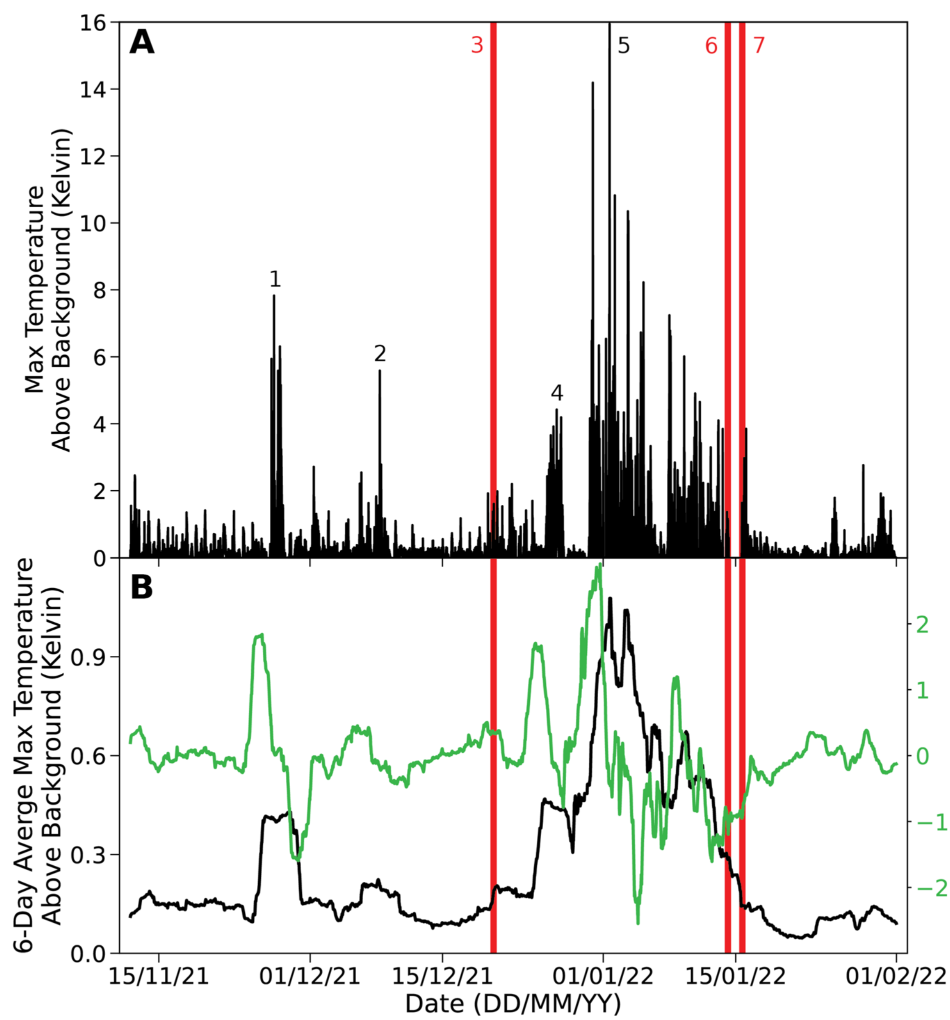

Fig. 3 **A** Maximum temperature above background time series of HTHH. The numbers represent divergent thermal events (or large changes in retrieved anomaly temperatures) and red indicates the major explosive eruptions. **B** Smoothed temperature trend over a 6-day period showing the maximum temperature above background (black line) and its derivative over a 24-h period (green line). The 6-day period is used to remove any transient nonvolcanic thermal influences on the temporal record (Thompson et al. 2022). The 24-h period is chosen to highlight sustained changes in thermal trends but limiting the diurnal influence on results

temperature above background of 7.2 K was detected on 8 January, 6–7 days prior to the large explosive eruptions. High quantities of sulfur and water species were also detected during and after the 14–15 January 2022 eruption with minimal ash detected in the visually opaque portions of the eruption column.

Thermal trends

The first detected deviation from the thermal background at HTHH occurred on 28 and 30 November 2021. These were characterized by temperatures > 2 K above background over a sustained period (~ 6 h). During that initial time period, the maximum temperature above background increased to 6.6 K and coincided with an increase in the rate of temperature change to more than 2 K over 24 h (Fig. 3). This was followed by a second sustained anomaly event (10–11 December 2021) prior to the Surtseyan explosive eruptions on 20 December 2021. Again, an increase in the derivative was observed; however, this was not as large as the previous perturbation. Thermal activity at HTHH continued until 5 January 2022, with notable temperature perturbations observed on 27 and 31 December 2021 as well as on 1, 3, and 8 January 2022 (Fig. 3).

On 14 January, a much larger explosive eruption occurred (second vertical red line in Fig. 3) following a period of decreasing thermal output. However, thermal perturbations were detected in the hours leading up to the event. Temperatures increased from 0.2 to 3.1 K and the derivative increased by 0.8 in the 3 h prior to the explosions. On 15 January 2022, the largest explosive phase of the eruption occurred, with small thermal perturbations (> 4 K) prior to it. Maximum temperatures above background increased from 0.1 to 2.2 K prior to the onset of the explosion with temperatures reaching ~ 4 K above background several hours after the eruption began. The elevated thermal anomalies subsided within 6 h to background levels (~ 0.5 K).

Temperature and decorrelation stretch

The combined analysis of surface temperature and decorrelation stretch images refined for volcanic emissions (e.g., sulfur dioxide, water, and ash) in the plume provides a computationally quick approach to see the dynamic plume processes. During the 15 January Phreatoplinian explosive eruption, a ~ 700-km-diameter plume of volcanic gases, steam, and ash rose ~ 58 km in the atmosphere. The ABI TIR data were sampled at 20-min intervals and detected the rapid transition of ash to ice on timescales of minutes in the outer potions of the umbrella at mid-altitudes (Fig. 4). These species remained close to the ambient atmospheric temperature around the freezing point of water (273 K). High concentrations of ice were identified in the rapidly rising plume (Fig. 4), with darker portions likely indicating ash that was less ice covered during the initial ascent phase. The surface temperatures and composition of the HTHH islands and ocean around the islands were obscured completely during the early hours of the eruption.

Ash composition and particle size (opaque plume)

The ABI emissivity data were modeled, and the AVAL library Sakurajima andesite spectral endmember was found to be the best fit, with other andesitic ash samples (e.g., Santiaguito) providing relatively good fits (e.g., low RMS error) to the opaque plume-bearing pixels. The spectral deconvolution model produces an areal percentage per pixel for each particle size range of the compositional endmember chosen plus that of ice. The modeling was conducted for the first 7 h of the eruption, during the period when the ash was opaque to upwelling ground radiance. By 1220 UTC, however, the plume had become more transparent rendering the linear deconvolutional model invalid (Fig. 5).

The results (Fig. 5) show the mixture of the two most dominant ash particle sizes as well as water ice. The plume did show a range of particle sizes present in varying quantities over the plume's evolution where a retrieval was possible. Ice appears to coat the particles very quickly and is one of the dominant components of the plume throughout the analysis period. Additionally, the quantity of ice present appears to increase over time, indicating the continued coating of the ash with ice. Coarser particles are present within the plume particularly toward the beginning of the eruption; however, as the eruption advances, smaller particles become more prevalent. Areas around the eastern fringe of the plume were shown to have coarser particles (> 63 μm) almost exclusively; however, these areas are also associated with higher RMS errors (> 0.2 to > 1 in some areas) indicating model results that are less accurate.

Gas and ash detections (diffuse plume)

Modeling the diffuse (thermally transparent) part of the plume or drifting cloud that is more distal from the vent relies on the upwelling ground radiance transmitted through the plume. Tracking the physical and chemical evolution of HTHH eruption cloud's time series of BT_{max}, SO_2 index, and ash index maps provides insights into the slightly longer-term (12–24 h) physical and chemical evolution (Supplement S1, Fig. 6). In particular, we found a 17-h delay between the TIR-based detections of ash and SO_2. At 05:30 UTC on 15 January 2022 (Fig. 6a), approximately 90 min after the climactic explosive eruption of HTHH, the eruption column was characterized by

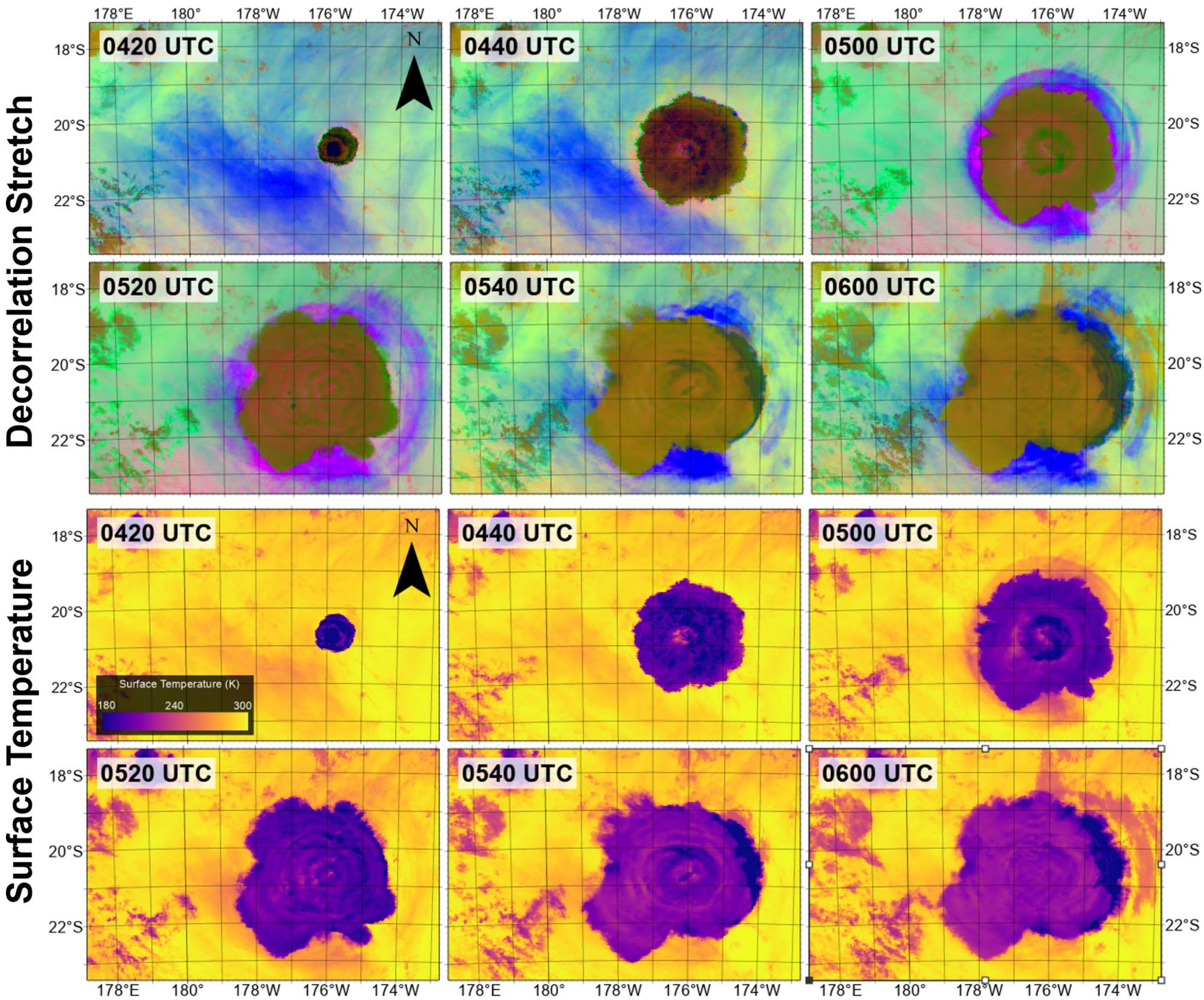

Fig. 4 Decorrelation stretch images (top two panels) of GOES ABI radiance bands 15, 14, and 11 (R, G, B) on 15 January 2022 (time in UTC) showing the rapid transition of water vapor (liquid) to ice (magenta to blue colors) in the outer portions of the umbrella cloud during ascent into the atmosphere. The opaque portion of the plume (brown to yellow) are concentrated with ash and ice-coated ash particles. Brightness temperature (bottom two panels) calculated using GOES ABI radiance band 14 showing the rapid cooling of the cloud by the first time step

low BT_{max} and ash absorption. Because we screen the ash (and SO_2) index maps for the presence of ice-phase clouds (Krotkov et al. 2021), we attribute the low BT_{max} and ash index to the high optical depth of the eruption clouds. We infer that ash obscured the presence of SO_2 during the first 90 min following the explosive eruption.

At 16:30 UTC (Fig. 6b), the dispersion of the eruption column (red oval) further reduced the optical depth in the margins of the plume, leading to rims of higher temperatures and ash index values around the core of the eruption column. This interpretation is consistent with the eruption chronology of Gupta et al. (2022), who reported two distinct umbrella clouds, and the westward transit of the upper umbrella (~ 30-km altitude) exposing the lower umbrella (~ 17-km altitude) over time.

At 11:30 UTC on 16 January 2022 (Fig. 6d), the SO_2 cloud reached the coast of Australia, approximately 1750 km from the previous position near New Caledonia. We expect the strength of SO_2 absorption to increase with view zenith angle (VZA), due to the corresponding increase in the length of the optical path through the eruption clouds. The observed increase in the strength of the SO_2 absorption was more likely due to the increase in VZA (82.5° vs. 67.5°) rather than any increase in the concentrations of SO_2 during its transit from the volcano across the Coral Sea.

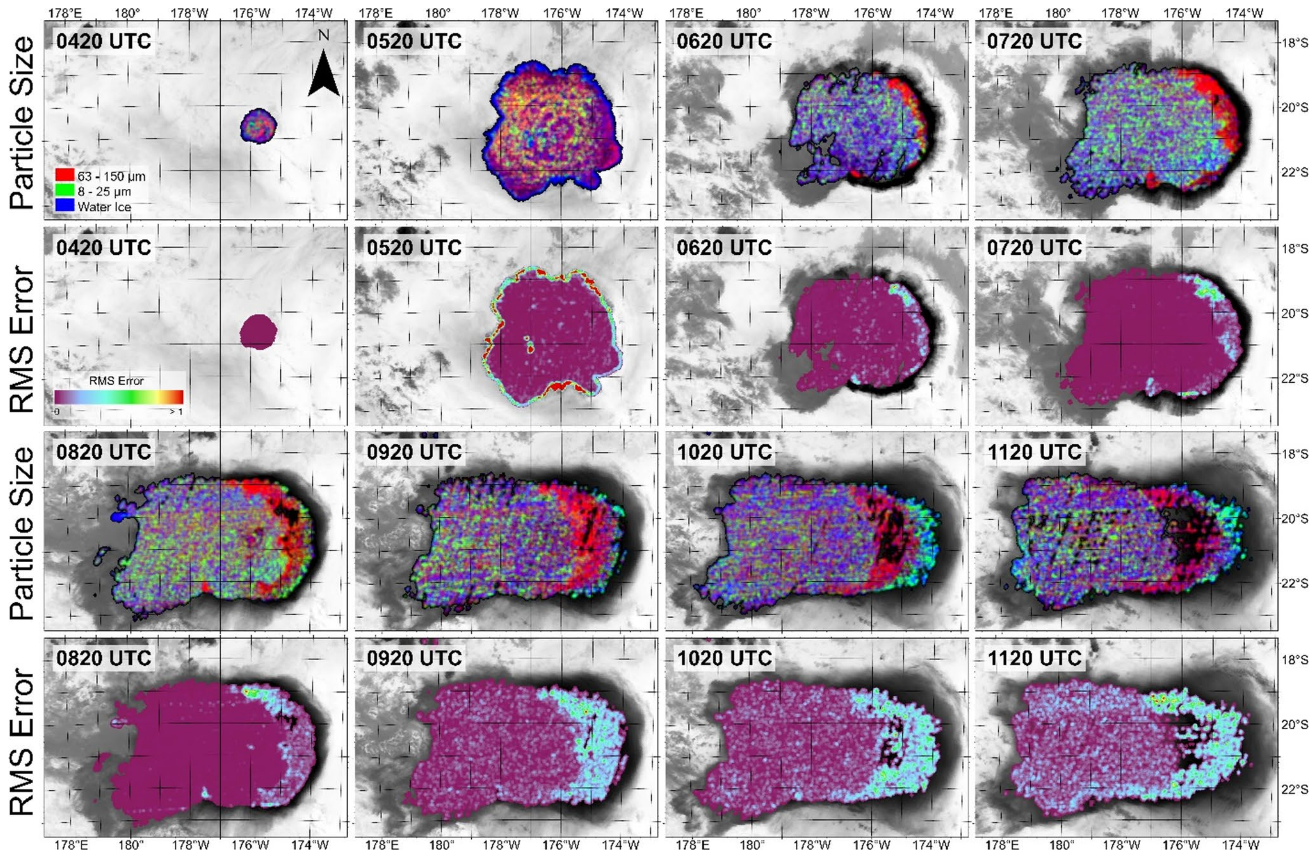

Fig. 5 Results of the linear deconvolution analysis of the opaque plume, along with accompanying RMS errors on 15 Jan 2022. Data are shown here at 1-h intervals. Red, green, or a combination thereof (yellow) all indicated pixels dominated by ash. Blue, magenta, and cyan colors represent pixels dominated by ice or ice plus ash

The preceding time series illustrated the changes in the optical depth of the HTHH eruption clouds due to the loss of ash. We obtain an additional constraint on the rate of these changes through an analysis of the cloud optical depth (COD), which is generated by the GOES-R Daytime Cloud Optical and Microphysics Properties (DCOMP) retrieval procedure (Walther and Heidinger 2012; Heidinger et al. 2020). A sequence of five COD maps (Fig. 7) documents the rapid (4-h) decrease in the area of HTHH ash clouds that we attribute to the loss of ash. The COD was not designed to map ash or sulfate aerosols explicitly, but changes in the COD can track changes in the ash or sulfate content of volcanic clouds.

The first COD map in our sequence (Fig. 7a) was generated from the ABI observation at 13:30 UTC, 15 January 2022, acquired approximately 9.5 h after the onset of the climactic explosive eruption. The ash-rich eruption clouds are characterized by COD > 8, and we used this contour line to describe the area of the ash clouds. The 13:30 cloud was the reference for estimating the relative reduction in the area over time. The second COD map (Fig. 7b), corresponding to the ABI observation at 14:30 UTC, indicates a relative reduction of 12% in the area of the ash cloud. The relative reduction was 33% by 15:30 UTC (Fig. 7c), 49% by 16:30 UTC (Fig. 7d), and 66% by 17:30 UTC (Fig. 7e). The relative reduction in area was approximately linear (Fig. 7f), with a loss rate of 16.6% per hour. This suggests a rapid loss of ash, but the loss in the area is only a constraint, or bound, on the volumetric loss of ash.

Discussion

Thermal precursors

There are detected thermal fluctuations at HTHH weeks before the first Surtseyan eruptions in December 2021, even though the thermal fluctuations do not appear to correlate with the magnitude nor onset of the eruptive activity (Fig. 3). The statistically significant increase in maximum temperature in late November and early December are seen as indicators that the HTHH volcanic system was changing. The increased thermal output raised the water/land average temperature by 5–7 K above the average (points 1 and 2 in Fig. 3A). Thermal

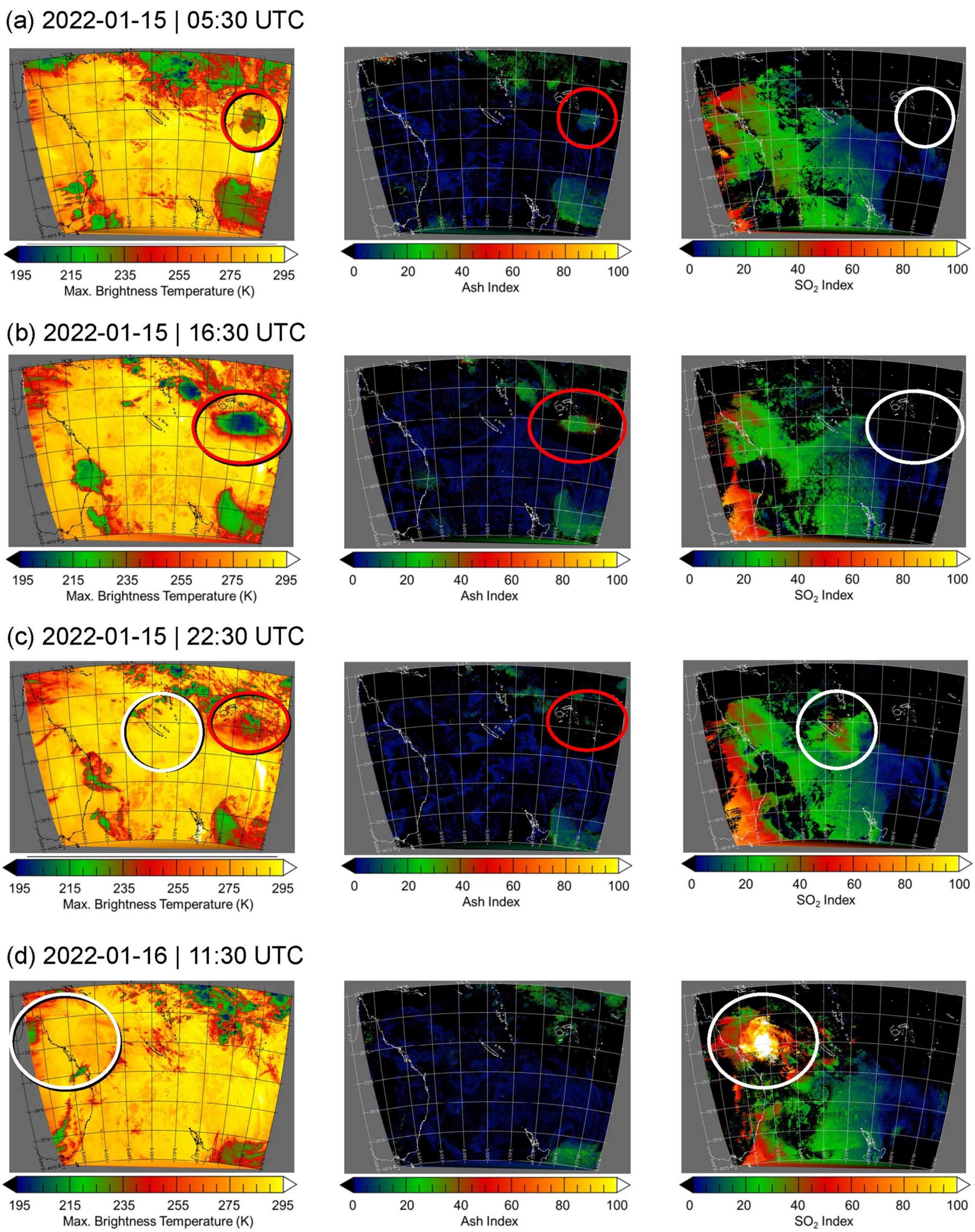
(a) 2022-01-15 | 05:30 UTC
195 215 235 255 275 295
Max. Brightness Temperature (K)
0 20 40 60 80 100
Ash Index
0 20 40 60 80 100
SO2 Index
(b) 2022-01-15 | 16:30 UTC
195 215 235 255 275 295
Max. Brightness Temperature (K)
0 20 40 60 80 100
Ash Index
0 20 40 60 80 100
SO2 Index
(c) 2022-01-15 | 22:30 UTC
195 215 235 255 275 295
Max. Brightness Temperature (K)
0 20 40 60 80 100
Ash Index
0 20 40 60 80 100
SO2 Index
(d) 2022-01-16 | 11:30 UTC
195 215 235 255 275 295
Max. Brightness Temperature (K)
0 20 40 60 80 100
Ash Index
0 20 40 60 80 100
SO2 Index

Fig. 6 The SO_2 signal in the plume (right column) was obscured by ash in the first 17 h following the climactic explosive eruption of HTHH. Red oval: ash, white oval: SO_2. **a** Approximately 90 min after the onset of the explosion and the eruption column is identified by low brightness temperatures and a weak signal (low absorption) in the ash index map, with no expression in the SO_2 index map. **b** Dispersion of the eruption column has led to rims of higher temperatures and ash index values around the opaque core of the eruption column. **c** The ash cloud can still be discerned in the temperature map, but the ash index was removed by the meteorological cloud screening, suggesting that the remaining ash was coated with ice. The SO_2 index indicates moderate absorption in the vicinity of New Caledonia. **d** The SO_2 cloud has reached the coast of Australia. The increase in the strength of the SO_2 absorption was more likely due to the increase in satellite view angle (82.5° vs. 67.5°) rather than any increase in the concentrations of SO_2

activity returned to background levels for a period of time and slowly started to increase again prior to the Surtseyan eruptions (point 3 in Fig. 3A). Those eruptions were followed by a period of rapid thermal fluctuations (points 4 and 5 in Fig. 3A) as seen in the derivative plot in Fig. 3B. Although fluctuating, the average temperature decreased over this period returning to an increased maximum temperature in several scenes just prior to the large explosive eruption on 14 January 2022 (points 6 and 7 in Fig. 3A).

The HTHH volcano is predominantly submarine, with only two small subaerial islands available to analyze for thermal fluctuations, resulting in a high proportion of the pixel containing the ocean surface. This makes it difficult to develop a reliable baseline trend in thermal activity as the surrounding ocean can dampen any thermal anomalies detected on the land surface; however, a maximum average temperature is used to minimize the influence of the background. Once the eruptions began, the large volcanic plumes rose and expanded into the atmosphere blocking any observations of the surface temperature. Furthermore, these plumes rapidly cooled in the upper atmosphere, which further obscures the thermal signatures of the ejected ash and volatiles within minutes. The highest thermal anomalies and radiant heat flux detected at HTHH were observed in early January 2022 during the building of the combined HTHH island and prior to its subsequent destruction in 14–15 January 2022. Ultimately, high-temporal-resolution TIR data used for thermal trend analyses on submarine-subaerial island volcanoes present a challenge to current detection capabilities; however, some insights into activity can be assessed based on the derivative of the thermal trend to highlight significant divergencies from the background.

Ash evolution

The development of the ash cloud structure has been well documented, with the plume reaching altitudes not observed in the satellite era (i.e., the mesosphere; Carr et al. 2022; Proud et al. 2022). Our analysis allows us to observe the distribution of ash and ice along the opaque plume top. Based on comparison with these height measurements, the region of the plume with highest optical depth for the spectral deconvolution analysis was in the upper umbrella cloud that rose to a height of ~ 34 km before spreading laterally. The plume was a mixture of ash and water vapor initially, which has been documented in previous studies (e.g., Khaykin et. al., 2022; Millán, et al. 2022). Our results show that ash was a significant component at the onset of the 15 January paroxysmal eruption (Fig. 5, 0420 to 0520 UTC). As one would expect, the proximal plume is initially a complex mixture of various particle sizes from the initial explosion combined with water vapor. This ash served as nucleation sites for the water vapor to precipitate, cool, and form ice coatings at higher altitudes. This leads to a gradual damping of the silicate detection replaced by that of ice, which we observe in the TIR spectra. The amount of water vapor/ice injected into the stratosphere was estimated to be 70–150 Tg (Khaykin et. al. 2022). This nucleation processes happened rapidly, with ice becoming the dominant spectral endmember at the opaque plume top within the first 2 h of the eruption (Fig. 5, 0620 UTC). The areal percentage of ice continued to increase over the eruptive sequence and spreading of the plume. As the ash cloud drifted further west, a change from coarser ash (> 63 µm) particles to the dominance of very fine (< 45 µm) particles at the plume top is seen between 0720 and 0920 UTC, as the larger particles fell out of suspension. Furthermore, we assume a greater quantity of fine versus coarse particles because of the eruption's high explosivity and greater degree of magma fragmentation. Ice remained the dominant endmember; however, as the eruption continued, it almost fully dominates the plume top after 0920 UTC. Beyond ~ 1220 UTC, no part of the plume has a high enough particle density to be optically opaque, and the spectral deconvolution modeling approach becomes invalid. At this point, radiative transfer (RT) modeling becomes the appropriate model from which SO_2 and ash indices as well as quantitative SO_2 concentrations can be retrieved.

SO_2 evolution

Assuming that the conversion of SO_2 gas to sulfate aerosol results in an increase in optical depth, our interpretation that the optical depth of the eruption clouds decreased on the scale of hours appears to contradict reports of the rapid conversion of SO_2 to sulfate aerosols (e.g., Baron et al. 2023; Bourassa et al. 2023; Carn et al. 2022; Sellitto et al. 2022, 2024; and Zhu et al. 2022). However, the loss of SO_2 operates at much slower rates than the loss of ash recorded by the COD time series (Fig. 7), as these investigators estimated e-folding times (i.e., time required to reduce SO_2 mass by a factor of 2.72) between 6 and 15 days.

Figure 6c and d show the sequence of BT_{max} and SO_2 index maps of the diffuse plume and highlight that SO_2 was

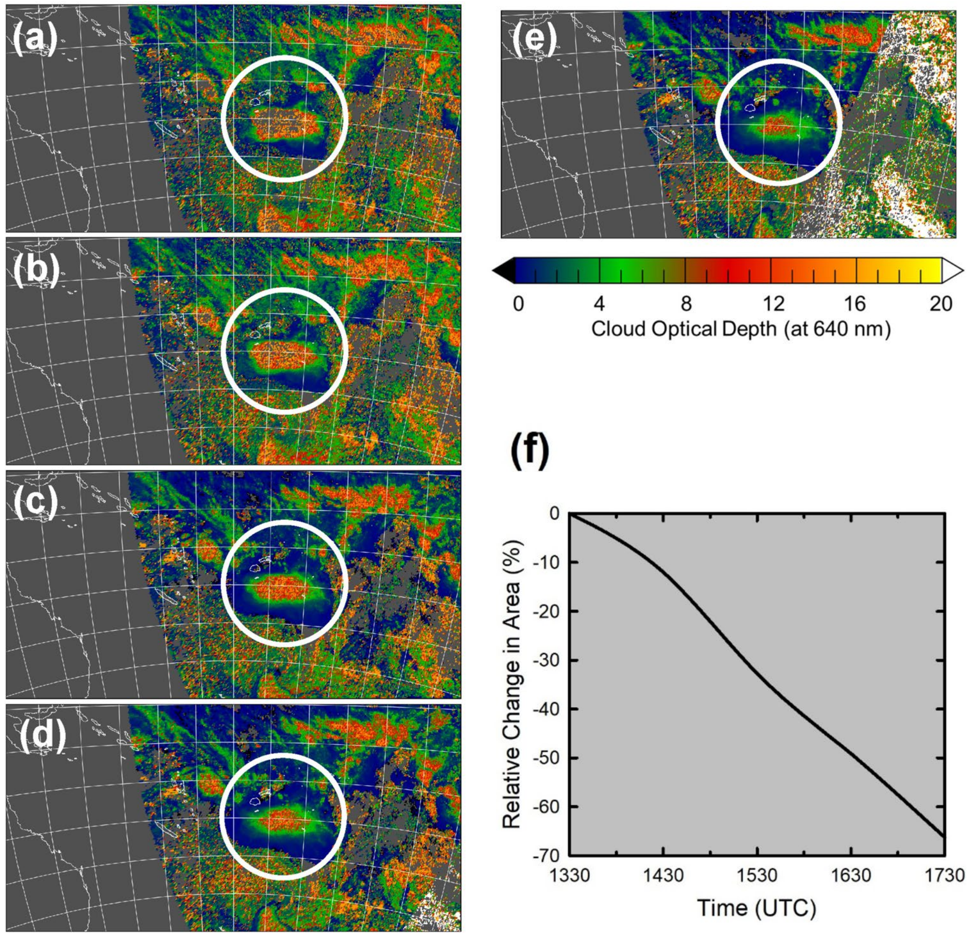

Fig. 7 Rapid (4-h) decrease in the area of HTHH ash cloud, as documented by GOES-R Daytime Cloud Optical and Microphysics Properties (DCOMP) retrieval. The decrease in area represents the decrease in the cloud optical depth (COD) as ash fell out of the drifting cloud. (**a**) ABI observation at 13:30 UTC, 15 Jan 2022, approximately 9.5 h after the onset of the climactic explosive eruption. We used this cloud as the reference for our estimates of the reduction in the cloud area. (**b**) Observation at 14:30 UTC. (**c**) Observation at 15:30 UTC. (**d**) Observation at 16:30 UTC. (**e**) Observation at 17:30 UTC. (**f**) The reduction in cloud area was approximately linear

not detected until ~ 22:30 UTC on 15 January 2022—11 h after the last time frame in Fig. 5. The quantitative retrieval of SO_2 requires an estimate of plume height to define the temperature contrast between the plume and underlying radiating surface (cf., Realmuto and Berk 2016). We estimated the height of the SO_2 clouds based on the dispersion and transport of the clouds. The clouds traveled 1750 km to the west (heading of 263.4 deg) in the 12 h between 23:30 on 15 January 2022 and 11:30 UTC on 16 January 2022 (Supplement S1), corresponding to a transport rate of 40.5 m/s. We note that this estimate is a lower limit on the rate of plume transport as the map projection applied to the ABI data does not incorporate the height of the plumes.

We compared this rate of transport to E–W wind speed profiles from the MERRA-2 (Rienecker et al. 2011) archive (Fig. 8) interpolated to the midpoint of the westward transit of the HTHH SO_2 clouds. The windspeed profiles for 22:30 UTC on 15 January 2022 (Fig. 8a), 04:30 UTC (Fig. 8b), and 10:30 UTC on 16 January 2022 (Fig. 8c) indicated speeds of 40.5 m/s at altitudes between 35 and 40 km. This height estimate agrees with estimates of cloud heights based on stereo imaging (Carr et al. 2022; Proud et al. 2022) and cloud-top temperature (Gupta et al. 2022). Therefore, we used a cloud height of 40 km in our RT-based mapping of SO_2 column density.

Our quantitative estimates of SO_2 column density (Fig. 9) were retrieved from the Plume Tracker model (Realmuto and Berk 2016) and made use of new capabilities for assessing the optical depth along individual LOS. These assessments are based on comparisons of surface temperature estimates with the air temperature at the surface elevation. If the estimate of surface temperature is lower than the air temperature, we assume that the LOS passed through features, such as ash and meteorological clouds, with significant optical depth.

We analyzed the ABI data acquired at 07:30 UTC on 16 January 2022 to derive the SO_2 column density. The analysis was challenging due to the combination of cloudy viewing conditions, a humid tropical atmosphere, and the very large VZA of the data containing the drifting cloud. Observing at large VZA increases the optical path through the atmosphere, leading to increases in the absorption of radiance along the optical paths. Specifically, the SO_2 clouds were viewed at VZA between 70 and 80° (Fig. 9a). The SO_2 index map (Fig. 9b) shows enhanced SO_2 and water vapor absorption due to the long optical paths. The prominent gaps or

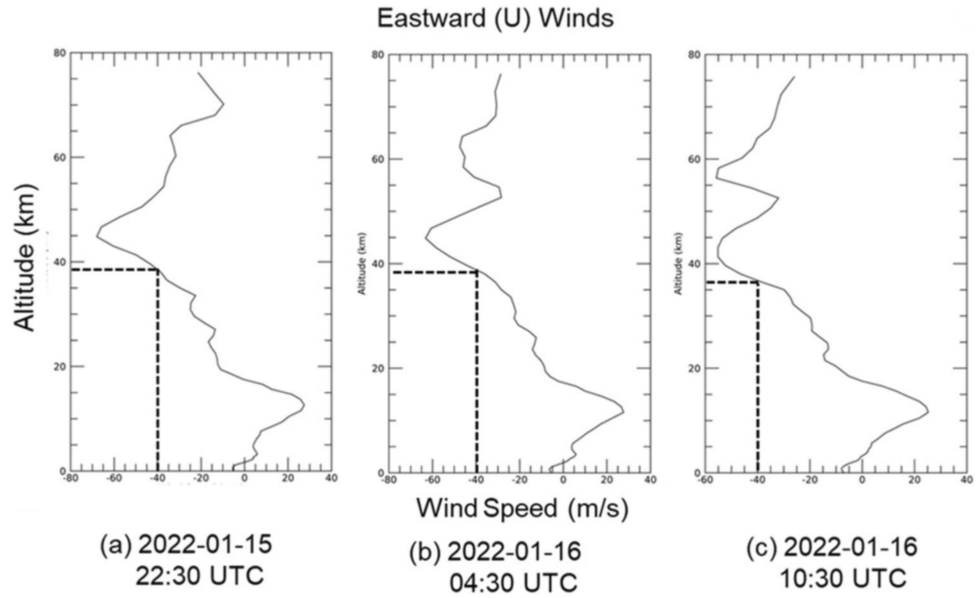

Fig. 8 Estimation of height of HTHH SO_2, based on dispersion and transport of the volcanic clouds. The clouds traveled 1750 km to the west (heading of 263.4 deg) in the 12 h between 23:30 on 15 Jan 2022 and 11:30 UTC on 16 Jan 2022, corresponding to a transport rate of 40.5 m/s. Comparing this rate to MERRA-2 wind speed profiles at (**a**) 22:30 UTC on 15 Jan 2022, and (**b**) 04:30 UTC and (**c**) 10:30 UTC on 16 Jan 2022 (dashed lines) indicates cloud heights between 35 and 40 km. We used a cloud height of 40 km in our RT-based mapping of SO_2 column abundance

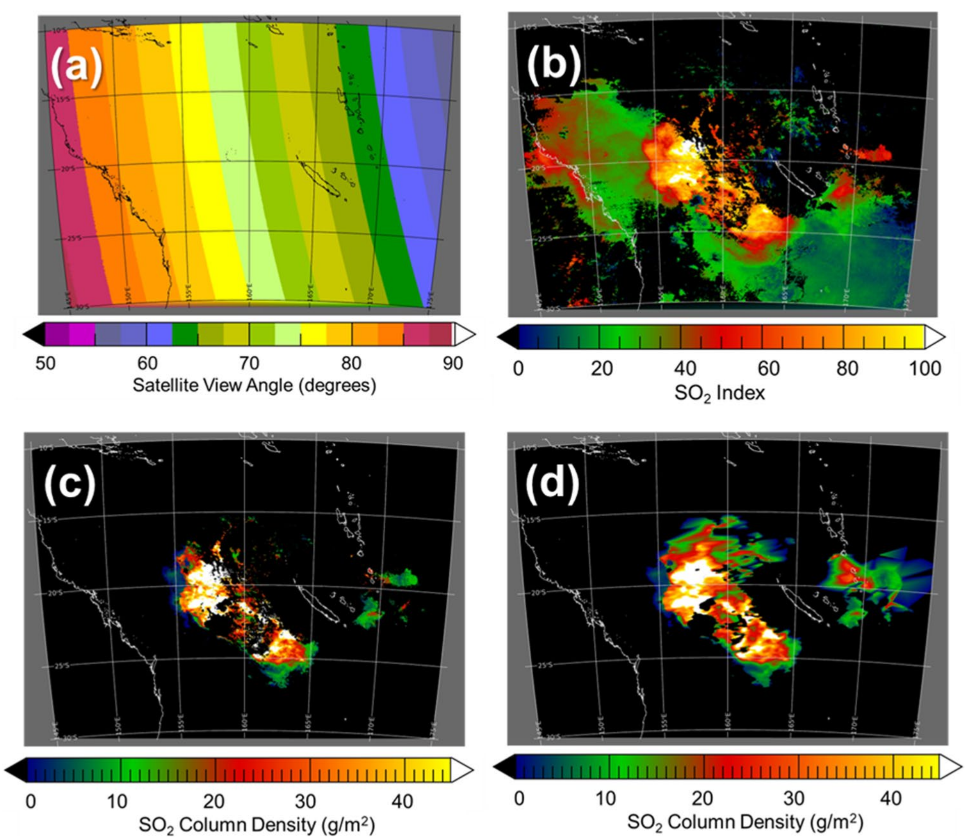

Fig. 9 The RT-based mapping of the HTHH SO_2 clouds. **a** Map of VZA, indicating that the SO_2 clouds were viewed at very large VZA between 70 and 80°. **b** SO_2 index image for 0730 UTC on 16 Jan 2022 showing strong SO_2 absorption. The index incorporates a mask for ice-phase clouds, which resulted in gaps in the plume. **c** SO_2 column density image. The prominent gaps in the SO_2 map are the result of the initial ice cloud screen plus an RT-based screening for high values of optical depth. **d** Reconstructed SO_2 column density image

holes in the map of SO_2 column density (Fig. 9c) map are the combined results of ice-phase cloud screening by the SO_2 index and optical depth screening by Plume Tracker. We "repair" the map (Fig. 9d) by interpolating values over the gaps through the triangulation of SO_2 retrievals surrounding those gaps.

We estimated a total SO_2 mass of 0.45 Tg released on 15 January, in agreement with UV-based estimates from Carn et al. (2022) and Duchamp et al. (2023), as well as the TIR-based estimates from Sellitto et al. (2024). This mass of SO_2 is low relative to eruptions of similar magnitude at other volcanoes, which is attributed to scrubbing of the submarine SO_2 emissions (Carn et al. 2022) and rapid conversion to sulfate aerosols due to the injection of water vapor into the upper atmosphere (Baron et al. 2023; Bourassa et al. 2023; Carn et al. 2022; Legras et al. 2022; Sellitto et al. 2024; and Zhu et al. 2022). Our analysis of the ABI time-series data suggests a third mechanism: the high optical depth of ash-rich eruption clouds limited the detection and mapping of SO_2 in the ~ 17 h following the climactic explosive eruption. This phenomenon of ash obscuring the presence of SO_2 would affect both UV and TIR-based mapping of SO_2.

Conclusions

High-temporal-resolution TIR data from geostationary sensors made possible using integrated sensor web detection of the large HTHH volcanic eruption enabled a complete time-series study of that eruption, a first at a submarine volcano. Notably, we show the applicability of the data analysis for the pre-, syn-, and post-eruption sequence. Temperature and heat flux trends were captured prior to the eruption showing measurable deviation from the background 2 weeks prior to the first Surtseyan eruption and more than 6 weeks prior to the larger explosive eruption. Although not directly attributed to a precursor of a particular eruption, our results do definitely show that lower spatial, higher temporal resolution geostationary TIR data are useful to detect thermal changes. This is particularly useful for remote volcanoes (including submarine centers) where several weeks of warning time could be critically important.

Following the eruption onset, TIR spectral deconvolution modeling of the opaque plume retrieved the ash composition and particle size together with the fraction of water ice. As the plume spread and became increasingly transparent, the deconvolution modeling became invalid in favor of the RT-based SO_2 retrieval analysis to track and estimate the SO_2 concentration as the cloud drifted to the coast of Australia. The temperature and composition of the gas and ash plume evolved over time. During the explosive phase, the initial release of water vapor was followed by the increased detection of volcanic ash. Ice then began to coat the ash particles as the plume drifted. The later detection and lower amount of SO_2 retrieved was found to be most likely due to obscuration by the ash-rich plume in the first 12 h of the eruption rather than another mechanism involving water. The opportunity exists to use this method operationally at other submarine/remote volcanoes that fall within the observational footprint of each geostationary TIR sensor.

Supplementary Information The online version contains supplementary material available at https://doi.org/10.1007/s00445-025-01901-5.

Author contributions James O. Thompson: conceptualization, formal analysis, investigation, methodology, software, visualization, writing—original draft. Daniel B. Williams: formal analysis, investigation, methodology, visualization, writing—original draft and editing. Michael S. Ramsey: funding acquisition, project administration, writing—review and editing. Vince Realmuto: formal analysis, investigation, methodology, visualization, writing—original draft.

Funding This research is funded by NASA grant 80NSSC20K1336 awarded under the Earth Science Research from Operational Geostationary Satellite Systems Program to MSR.

Data availability The thermal analysis code is available on GitHub at https://github.com/jthompson2710/VolcanoURP-GOES16 (DOI: available at publication), with the data available through the NOAA S3 Amazon Web Server (for example: https://noaa-goes16.s3.amazonaws.com/index.html). The Plume Tracker software is available through Limited Release. Please contact vincent.j.realmuto@jpl.nasa.gov for more information.

Declarations

Conflict of interest The authors declare that they have no known competing financial interests or personal relationships that could have appeared to influence the work reported in this paper. The funders had no role in the design of the study; in the collection, analyses, or interpretation of data; in the writing of the manuscript; or in the decision to publish the results.

Ethical approval Not applicable.

References

Acker JG, Leptoukh G (2007) Online analysis enhances use of NASA earth science data. Eos Trans AGU 88(2):14–17. https://doi.org/10.1029/2007EO020003

Ackerman SA, Schreiner AJ, Schmit TJ et al (2008) Using the GOES sounder to monitor upper level SO_2 from volcanic eruptions. J Geophys Res Atmos 113:D14. https://doi.org/10.1029/2007JD009622

Baron A, Chazette P, Khaykin S et al (2023) Early evolution of the stratospheric aerosol plume following the 2022 Hunga Tonga-Hunga Ha'apai eruption: lidar observations from Reunion (21°S, 55°E). Geophys Res Lett 50:e2022GL101751. https://doi.org/10.1029/2022GL101751

Boichu M, Grandin R, Blarel L et al (2023) Growth and global persistence of stratospheric sulfate aerosols from the 2022 Hunga Tonga-Hunga Ha'apai volcanic eruption. J Geophys Res Atmos 128(23):e2023JD039010. https://doi.org/10.1029/2023JD039010

Bourassa AE, Zawada DJ, Rieger LA et al (2023) Tomographic retrievals of Hunga Tonga-Hunga Ha'apai volcanic aerosol. Geophys Res Lett 50:e2022GL101978. https://doi.org/10.1029/2022GL101978

Brenna M, Cronin SJ, Smith IEM et al (2022) Post-caldera volcanism reveals shallow priming of an intra-ocean arc andesitic caldera: Hunga volcano, Tonga, SW Pacific. Lithos 412:106614. https://doi.org/10.1016/j.lithos.2022.106614

Bryan WB, Stice GD, Ewart A (1972) Geology, petrography, and geochemistry of the volcanic islands of Tonga. J Geophys Res 77:1566–1585. https://doi.org/10.1029/jb077i008p01566

Carn SA, Krotkov NA, Fisher BL, Li C (2022) Out of the blue: volcanic SO_2 emissions during the 2021–2022 eruptions of Hunga Tonga-Hunga Ha'apai (Tonga). Front Earth Sci 10:976962. https://doi.org/10.3389/feart.2022.976962

Carr JL, Horváth Á, Wu DL, Friberg MD (2022) Stereo plume height and motion retrievals for the record-setting Hunga Tonga-Hunga Ha'apai eruption of 15 January 2022. Geophys Res Lett 49(9):e2022GL098131. https://doi.org/10.1029/2022GL098131

Conel JE (1969) Infrared emissivities of silicates: experimental results and a cloudy atmosphere model of spectral emission from condensed particulate mediums. J Geophys Res 74(6):1614–1634. https://doi.org/10.1029/JB074i006p01614

Cronin SJ, Brenna M, Smith IEM et al (2017) New volcanic island unveils explosive past. Eos (United States) 98:18–23. https://doi.org/10.1029/2017eo076589

Duchamp C, Wrana F, Legras B et al (2023) Observation of the aerosol plume from the 2022 Hunga Tonga-Hunga Ha'apai eruption with SAGE III/ISS. Geophys Res Lett 50:e2023GL105076. https://doi.org/10.1029/2023GL105076

Ellrod GP, Connell BH, Hillger DW (2003) Improved detection of airborne volcanic ash using multispectral infrared satellite data. J Geophys Res Atmos. https://doi.org/10.1029/2002jd002802

Garnier A, Pelon J, Dubuisson P et al (2013) Retrieval of cloud properties using CALIPSO imaging infrared radiometer. Part II: Effective diameter and ice water path. J Appl Meteorol Climatol 52:2582–2599. https://doi.org/10.1175/JAMC-D-12-0328.1

Gillespie A, Rokugawa S, Matsunaga T et al (1998) A temperature and emissivity separation algorithm for advanced spaceborne thermal emission and reflection radiometer (ASTER) images. IEEE Trans Geosci Remote Sens 36:1113–1126. https://doi.org/10.1109/36.700995

Girona T, Realmuto V, Lundgren P (2021) Large-scale thermal unrest of volcanoes for years prior to eruption. Nat Geosci 14:238–241. https://doi.org/10.1038/s41561-021-00705-4

Gupta AK, Bennartz R, Fauria KE, Mittal T (2022) Eruption chronology of the December 2021 to January 2022 Hunga Tonga – Hunga Ha'apai eruption sequence. Nature Comm 3:314. https://doi.org/10.1038/s43247-022-00606-3

Harris AJL (2013) Thermal remote sensing of active volcanoes: a user's manual, 1st edn. Cambridge University Press, New York

Heidinger AK, Pavolonis MJ, Calvert C et al (2020) ABI cloud products from the GOES-R series. In: Goodman SJ, Schmit TJ, Daniels J, Redmon RJ (eds) The GOES-R Series. Elsevier, Amsterdam, pp 43–62. https://doi.org/10.1016/B978-0-12-814327-8.00006-8

Khaykin S, Podglajen A, Ploeger F et al (2022) Global perturbation of stratospheric water and aerosol burden by Hunga eruption. Commun Earth Environ 3(1):316. https://doi.org/10.1038/s43247-022-00652-x

Krotkov N, Realmuto VJ, Li C et al (2021) Day-night monitoring of volcanic SO_2 and ash clouds for aviation avoidance at northern polar latitudes. Remote Sens 13:4003. https://doi.org/10.3390/rs13194003

Legras B, Duchamp C, Sellitto P et al (2022) The evolution and dynamics of the Hunga Tonga-Hunga Ha'apai sulfate aerosol plume in the stratosphere. Atmos Chem Phys 22(22):14957–14970. https://doi.org/10.5194/acp-22-14957-2022

Lundgren P, Girona T, Bato MG et al (2020) The dynamics of large silicic systems from satellite remote sensing observations: the intriguing case of Domuyo volcano, Argentina. Sci Rep 10:1–15. https://doi.org/10.1038/s41598-020-67982-8

Mackie S, Millington S, Watson IM (2014) How assumed composition affects the interpretation of satellite observations of volcanic ash. Meteorol Appl 21(1):20–29. https://doi.org/10.1002/met.1445

Meerdink SK, Hook SJ, Roberts DA, Abbott EA (2019) The ECOSTRESS spectral library version 1.0. Remote Sens Environ 230:111196. https://doi.org/10.1016/j.rse.2019.05.015

Millán L, Santee ML, Lambert A et al (2022) The Hunga Tonga-Hunga Ha'apai hydration of the stratosphere. Geophys Res Lett 49(13):e2022GL099381. https://doi.org/10.1029/2022GL099381

Millán L, Read WG, Santee ML et al (2024) The evolution of the Hunga hydration in a moistening stratosphere. Geophys Res Lett 51(19):e2024GL110841. https://doi.org/10.1029/2024GL110841

Pavolonis MJ, Heidinger AK, Sieglaff J (2013) Automated retrievals of volcanic ash and dust cloud properties from upwelling infrared measurements. J Geophys Res Atmos 118(3):1436–1458. https://doi.org/10.1002/jgrd.50173

Pavolonis MJ, Sieglaff J, Cintineo J (2015) Spectrally enhanced cloud objects—a generalized framework for automated detection of volcanic ash and dust clouds using passive satellite measurements: 1. Multispectral analysis. J Geophys Res Atmos 120(15):7813–7841. https://doi.org/10.1002/2014JD022968

Pavolonis MJ, Sieglaff J, Cintineo J (2015) Spectrally enhanced cloud objects—a generalized framework for automated detection of volcanic ash and dust clouds using passive satellite measurements: 2. Cloud object analysis and global application. J Geophys Res Atmos 120(15):7842–7870. https://doi.org/10.1002/2014JD022969

Pavolonis MJ, Sieglaff JM, Cintineo JL (2020) Remote sensing of volcanic ash with the GOES-R series. In: Goodman SJ, Schmit TJ, Daniels J, Redmon RJ (eds) The GOES-R Series. Elsevier, Amsterdam. pp 103–124. https://doi.org/10.1016/B978-0-12-814327-8.00010-X

Prata AJ (1989) Observations of volcanic ash clouds in the 10–12 μm window using AVHRR/2 data. Int J Remote Sens 10(4–5):751–761. https://doi.org/10.1080/01431168908903916

Prata AJ, Grant IF (2001) Retrieval of microphysical and morphological properties of volcanic ash plumes from satellite data: application to Mt Ruapehu, New Zealand. Q J R Meteorolog Soc 127(576):2153–2179. https://doi.org/10.1002/qj.49712757615

Prata F, Bluth G, Rose B, Schneider D, Tupper A (2001) Comments on "Failures in detecting volcanic ash from a satellite-based technique." Remote Sens Environ 78(3):341–346. https://doi.org/10.1016/S0034-4257(01)00231-0

Proud SR, Prata AT, Schmauß S (2022) The january 2022 eruption of Hunga Tonga-Hunga Ha'apai volcano reached the mesosphere. Science 378:554–557. https://doi.org/10.1126/science.abo4076

Ramsey MS (2016) Synergistic use of satellite thermal detection and science: a decadal perspective using ASTER. In: Harris AJL, De Groeve T, Garel F, Carn SA (eds) Detecting, modelling and responding to effusive eruptions. Geological Society, London. pp 115–136. https://doi.org/10.1144/SP426

Ramsey MS, Christensen PR (1998) Mineral abundance determination: quantitative deconvolution of thermal emission spectra. J Geophys Res Solid Earth 103:577–596. https://doi.org/10.1029/97jb02784

Ramsey MS, Flynn ITW (2020) The spatial and spectral resolution of ASTER infrared image data: a paradigm shift in volcanological remote sensing. Remote Sens 12:738. https://doi.org/10.3390/rs12040738

Realmuto VJ, Berk A (2016) Plume tracker: interactive mapping of volcanic sulfur dioxide emissions with high-performance radiative transfer modeling. J Volcanol Geotherm Res 327:55–69. https://doi.org/10.1016/j.jvolgeores.2016.07.001

Rienecker MM, Suarez MJ, Gelaro R et al (2011) MERRA: NASA's modern-era retrospective analysis for research and applications. J Clim 24(14):3624–3648. https://doi.org/10.1175/JCLI-D-11-00015.1

Rose WI, Delene DJ, Schneider DJ et al (1995) Ice in the 1994 Rabaul eruption cloud: implications for volcano hazard and atmospheric effects. Nature 375(6531):477–479. https://doi.org/10.1038/375477a0

Ruff SW, Christensen PR, Barbera PW, Anderson DL (1997) Quantitative thermal emission spectroscopy of minerals: a laboratory technique for measurement and calibration. J Geophys Res Solid Earth 102:14899–14913. https://doi.org/10.1029/97jb00593

Schmit TJ, Griffith P, Gunshor MM et al (2017) A closer look at the ABI on the GOES-R series. Bull Am Meteorol Soc 98(4):681–698. https://doi.org/10.1175/BAMS-D-15-00230.1

Schoeberl MR, Wang Y, Taha G, Zawada DJ, Ueyama R, Dessler A (2024) Evolution of the climate forcing during the two years after the Hunga Tonga-Hunga Ha'apai eruption. J Geophys Res Atmos 129(14):e2024JD041296. https://doi.org/10.1029/2024JD041296

Sellitto P, Podglajen A, Belhadji R et al (2022) The unexpected radiative impact of the Hunga Tonga eruption of 15 January 2022. Nature Comm 3:288. https://doi.org/10.1038/s43247-022-00618-z

Sellitto P, Siddans R, Belhadji R et al (2024) Observing the SO_2 and sulfate aerosol plumes from the 2022 Hunga eruption with the Infrared Atmospheric Sounding Interferometer (IASI). Geophys Res Lett 51(19):e2023GL105565

Simpson JJ, Hufford G, Pieri D, Berg J (2000) Failures in detecting volcanic ash from a satellite-based technique. Remote Sens Environ 72(2):191–217. https://doi.org/10.1016/S0034-4257(99)00103-0

Taha G, Loughman R, Colarco PR et al (2022) Tracking the 2022 Hunga Tonga-Hunga Ha'apai aerosol cloud in the upper and middle stratosphere using space-based observations. Geophys Res Lett 49:e2022GL100091. https://doi.org/10.1029/2022GL100091

Thompson JO, Ramsey MS (2020) Spatiotemporal variability of active lava surface radiative properties using ground-based multispectral thermal infrared data. J Volcanol Geotherm Res 408:107077. https://doi.org/10.1016/j.jvolgeores.2020.107077

Thompson JO, Contreras-Arratia R, Befus KS, Ramsey MS (2022) Thermal and seismic precursors to the explosive eruption at La Soufrière Volcano, St. Vincent in April 2021. Earth Planet Sci Lett 592:117621. https://doi.org/10.1016/j.epsl.2022.117621

Vömel H, Evan S, Tully M (2022) Water vapor injection into the stratosphere by Hunga Tonga-Hunga Ha'apai. Science 377(6613):1444–1447. https://doi.org/10.1126/science.abq2299

Walther A, Heidinger AK (2012) Implementation of the daytime cloud optical and microphysical properties algorithm (DCOMP) in PATMOS-x. J Appl Meteorol Climatol 51:1371–1390. https://doi.org/10.1175/JAMC-D-11-0108.1

Williams DB, Ramsey MS (2019) On the applicability of laboratory thermal infrared emissivity spectra for deconvolving satellite data of opaque volcanic ash plumes. Remote Sens 11(19):2318. https://doi.org/10.3390/rs11192318

Williams DB, Ramsey MS (2022) Analysis of ash emissions from the 2020 Nishinoshima eruption using ASTER thermal infrared orbital data. J Volcanol Geotherm Res 421:107424. https://doi.org/10.1016/j.jvolgeores.2021.107424

Wilmouth DM, Østerstrøm FF, Smith JB, Anderson JG, Salawitch RJ (2023) Impact of the Hunga Tonga volcanic eruption on stratospheric composition. Proc Natl Acad Sci 120(46):e2301994120. https://doi.org/10.1073/pnas.2301994120

Yuen DA, Scruggs MA, Spera FJ et al (2022) Under the surface: pressure-induced planetary-scale waves, volcanic lightning, and gaseous clouds caused by the submarine eruption of Hunga Tonga-Hunga Ha'apai volcano. Earthq Res Adv 2:100134. https://doi.org/10.1016/j.eqrea.2022.100134

Zhu Y, Bardeen CG, Tilmes S, et al (2022) Perturbations in stratospheric aerosol evolution due to the water-rich plume of the 2022 Hunga-Tonga eruption. Nature Comm 3:248. https://doi.org/10.1038/s43247022-00580-w

Publisher's Note Springer Nature remains neutral with regard to jurisdictional claims in published maps and institutional affiliations.